Phase coexistence in $CaCu_xMn_{7-x}O_{12}$ solid solutions

W. Sławiński[a], R. Przeniosło[a,*], I. Sosnowska[a], M. Bieringer[b], I. Margiolaki[c], A.N. Fitch[c], E. Suard[d]

[a]*Institute of Experimental Physics, Warsaw University, Hoża 69, PL-00 681 Warsaw, Poland*
[b]*Department of Chemistry, University of Manitoba, Winnipeg, Manitoba, Canada R3T 2N2*
[c]*European Synchrotron Radiation Facility, BP 220, 38 043 Grenoble, France*
[d]*Institut Laue-Langevin, 6 rue Jules Horowitz, BP-156X 38 042 Grenoble, France*

Abstract

A phase diagram for $CaCu_xMn_{7-x}O_{12}$ for $x \leqslant 0.7$ is presented. At room temperature $CaCu_xMn_{7-x}O_{12}$ with $x = 0.10$ and 0.20 crystallizes in the trigonal space group $R\bar{3}$ and shows the same charge ordering of Mn^{3+} and Mn^{4+} ions as has been found for undoped $CaMn_7O_{12}$. The $x = 0.10$ and 0.20 compounds both show an apical-type Jahn–Teller distortion of the MnO_6 octahedra around Mn^{3+} ions. Both compounds undergo a structural phase transition to a high-temperature cubic structure (space group $Im\bar{3}$) with coexistence of both phases between 375 and 415 K for $x = 0.10$ and between 10 and 380 K for $x = 0.20$. The domain sizes of the coexisting phases are at least 200 nm for both $x = 0.10$ and 0.20 compounds.

1. Introduction

Manganese oxides are the subject of intense research efforts because of competing interactions which lead to the coupling of charge, spin, orbital and lattice degrees of freedom [1]. This interplay leads to various phenomena, like colossal magnetoresistance (CMR) [2], multiferroic properties [3,4] and colossal dielectric constants [5] which are interesting for basic science as well as for potential applications.

This paper deals with the manganite family of $CaCu_xMn_{7-x}O_{12}$ compounds with a distorted perovskite type crystal structure. The compound with the maximal Cu content ($x = 3$) $CaCu_3Mn_4O_{12}$ shows a magnetoresistance effect with a negative value of the magnetoresistivity (MR) MR $= -40\%$ [6]. Such a value is not very large as compared with MR observed in other manganites, see e.g. [1], but it has some remarkable features: MR weakly depends on the temperature and is large at RT and at

relatively low fields. $CaCu_3Mn_4O_{12}$ is also the first CMR material having only Mn^{4+} in the lattice [6], so the double exchange model assuming charge transfer between Mn^{3+} and Mn^{4+} ions could not be used to explain the CMR effect [6]. At smaller Cu doping values, when the $CaCu_xMn_{7-x}O_{12}$ lattice contains a mixture of Mn^{3+} and Mn^{4+} ions, the CMR effect was also observed with MR $= -34\%$ for $x = 2.5$ [7] and MR $= -60\%$ for $x = 1.0$ [8]. The MR values observed in $CaCu_xMn_{7-x}O_{12}$ at lower Cu doping for $x < 1$ decrease with decreasing x [9].

The parent undoped ($x = 0$) $CaMn_7O_{12}$ compound has a trigonal, charge ordered structure (space group $R\bar{3}$) [10] below 410 K and a cubic, charge delocalized structure (space group $Im\bar{3}$) above 450 K [11]. The atomic positions in both trigonal and cubic phases are shown in Table 1. Please note that the description of the structure will refer to the hexagonal setting of space group $R\bar{3}$ in agreement with numerous earlier studies [10–13]. A schematic representation of the trigonal unit cell of $CaCu_xMn_{7-x}O_{12}$ is shown in the rhombohedral setting of space group $R\bar{3}$ in Fig. 1. The rhombohedral setting is used to visualize some features of the structure—the hexagonal unit cell would be too large

*Corresponding author. Fax: +48 22 628 7252.
E-mail address: radek@fuw.edu.pl (R. Przeniosło).

Table 1
Positions of ions in the trigonal and cubic phases of $CaCu_xMn_{7-x}O_{12}$ compounds

Subl.	Label	Ions	Pos. ($R\bar{3}$)	x_h	y_h	z_h	Pos. ($Im\bar{3}$)	x_c	y_c	z_c
A	Ca	Ca^{2+}	(3a)	0	0	0	(2a)	0	0	0
A	Mn1	Mn^{3+}/Cu^{2+}	(9e)	1/2	0	0	(6b)	1/2	1/2	0
B	Mn2	Mn^{3+}/Mn^{4+}	(9d)	1/2	1/2	1/2	(8c)	1/4	1/4	1/4
B	Mn3	Mn^{4+}	(3b)	0	0	1/2	(8c)	1/4	1/4	1/4
O	O1	O^{2-}	(18f)	x_1	y_1	z_1	(24g)	x	y	0
O	O2	O^{2-}	(18f)	x_2	y_2	z_2				

Column 1 refers to the sublattices in the perovskite structure ABO_3. Columns 2 and 3 give the labelling and ions distribution in the trigonal phase as given in [10]. Column 4 refer to the crystallographic positions in the trigonal phase (space group $R\bar{3}$ in hexagonal setting). Columns 5–7 show the coordinates of ions in the hexagonal setting. Columns 8–11 show the corresponding crystallographic positions and coordinates in the cubic space group $Im\bar{3}$. The Mn and Cu ions in the B-sublattice are separated in the (9d) and (3b) sites in the trigonal phase but they merge into one (8c), mixed valence Mn/Cu site in the cubic phase. The O^{2-} ions in two different trigonal (18f) sites merge into one cubic (24g) site. The trigonal and cubic phases contain three and two $CaMn_7O_{12}$ formula units in the unit cell, respectively.

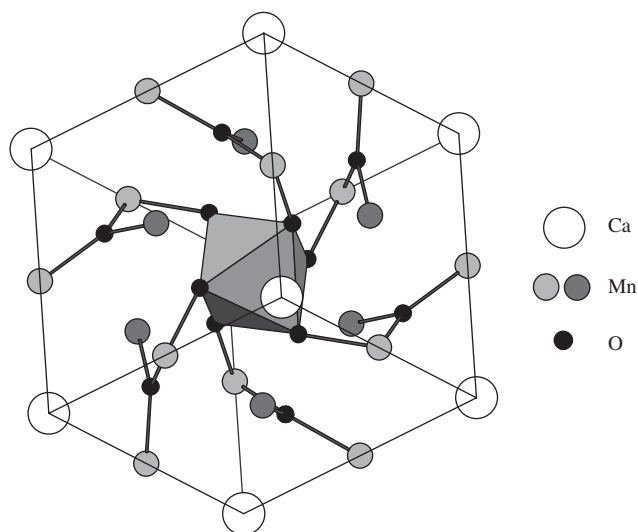Fig. 1. Schematic representation of the trigonal $CaCu_xMn_{7-x}O_{12}$ unit cell shown in the rhombohedral setting of space group $R\bar{3}$. The rhombohedral angle, $\alpha = 109.6°$, is taken from [10]. White and black circles denote Ca^{2+} and O^{2-} ions, respectively. Dark grey circles denote Mn1 positions occupied by a mixture of Mn and Cu ions. The light grey circles represent Mn ions in Mn2 positions. The central MnO_6 octahedron is regular and centred around the Mn^{4+} ion located in Mn3 positions. The network of Mn–O bonds shorter than 2.05 Å is shown with dark solid lines.

for this purpose. The central MnO_6 octahedron is regular and centred around the Mn^{4+} ion located in the Mn3 position in the centre of the rhombohedral unit cell. In the Ruddlesden–Popper phases [14], the Mn ions are only located on the B-sublattice, forming a network of corner sharing MnO_6 octahedra where each oxygen ion has two nearest neighbour Mn ions at a distance of about 2 Å. Whereas in $CaCu_xMn_{7-x}O_{12}$ the Mn/Cu ions are also located on the A-sublattice (position Mn1). As a consequence, oxygen ions are threefold coordinated by manganese ions with bond distances of about 2 Å, see Fig. 1.

Between 410 and 440 K large domains of both trigonal and cubic phases with at least 150 nm size coexist in the

$CaMn_7O_{12}$ material [11,12]. In the same temperature region (around 440 K) there is a remarkable jump of the $CaMn_7O_{12}$ resistivity [13,15] and Young modulus [13]. $CaMn_7O_{12}$ shows charge modulation below 250 K [16] and an anisotropic thermal lattice expansion with a local minimum of the c-lattice parameter at the same temperature range around 250 K [16]. These findings are closely related to giant dielectric constants of $CaMn_7O_{12}$ recently reported above 250 K [17]. The magnetic properties of $CaMn_7O_{12}$ are also unique. Below 90 K the Mn^{3+} and Mn^{4+} magnetic moments in $CaMn_7O_{12}$ are long-range ordered. The magnetic structure of $CaMn_7O_{12}$ is described with two magnetic phases: a ferrimagnetic and a modulated structure [18]. The coexistence of magnetic phases have been recently confirmed by μSR studies [19]. A magnetic phase transition associated with changes of the magnetic modulation lengths and magnetic ordering coherence length has been found around 49 K [20]. The magnetic ordering period changes from 32 up to 52 Å [20,21]. The anomalies at 49 and 89 K have been confirmed recently by magnetization, specific heat and dilatometric $CaMn_7O_{12}$ studies [22–24].

The Cu^{2+} ions introduced in the $CaCu_xMn_{7-x}O_{12}$ lattice are located in the Mn1 positions (see Table 1). The volume of the unit cell decreases with increasing Cu content [9,25–27]. Preliminary studies of $CaCu_xMn_{7-x}O_{12}$ compounds with small Cu doping of $x = 0.38$ have shown a phase coexistence [28] of a trigonal and a high-temperature cubic phase. The same compound with $x = 0.38$ also shows modulated magnetic ordering [29]. The main motivation of the present study was to observe the impact of small Cu doping levels on the structural phase transitions in the $CaCu_xMn_{7-x}O_{12}$ system for $x < 0.25$.

2. Materials and methods

2.1. Sample synthesis

Bulk samples of (approximately 5 g) of polycrystalline $CaCu_xMn_{7-x}O_{12}$ ($x = 0, 0.10, 0.20$) were prepared from

stoichiometric amounts of $CaCO_3$ (99.95% CERAC), CuO (99.999% CERAC) and Mn_2O_3 (99.99% CERAC). The combined starting materials were dissolved in concentrated nitric acid, the Mn_2O_3 only dissolved upon addition of 30 ml concentrated hydrogen peroxide solution. After co-precipitation of the metal oxides the solutions were evaporated to dryness. Heating for 4 h at 600 °C resulted in amorphous black solids. After addition of 10% KCl as a mineralizer the final product was obtained by annealing in oxygen at 850 °C for 13 h. The black products are highly crystalline phases and free of KCl [30]. The elemental compositions of the samples were determined by atomic emission spectroscopy (ICP-AES). The compositions of the $x = 0.10$ and 0.20 samples are $Ca_{1.00}Cu_{0.09(1)}Mn_{6.89(1)}O_{12}$ and $Ca_{1.00}Cu_{0.19(1)}Mn_{6.81(1)}O_{12}$, respectively.

2.2. Diffraction measurements

The neutron powder diffraction measurements of $CaCu_xMn_{7-x}O_{12}$ were performed using the diffractometer D20 at ILL Grenoble, operating at the neutron wavelength 1.306 Å. The measurements were performed at room temperature (RT) for three different polycrystalline $CaCu_xMn_{7-x}O_{12}$ samples with the nominal x Cu content: $x = 0.0, 0.10$ and 0.20. The samples were mounted in a 8 mm diameter vanadium container and the data acquisition time was 10 min for each sample. The neutron diffraction patterns were collected for the $10° < 2\theta < 72°$ range which corresponds to the $0.8 \text{Å}^{-1} < Q < 5.5 \text{Å}^{-1}$ scattering vector range.

Synchrotron Radiation (SR) powder diffraction was performed at the ID31 beamline, ESRF Grenoble, operating at wavelengths of 0.39996 and 0.40006 Å. The polycrystalline $CaCu_xMn_{7-x}O_{12}$ compounds with the nominal x Cu content: $x = 0.0, 0.10$ and 0.20 were mounted in a 0.5 mm diameter capillary. The measurements were performed at several temperatures above RT and one measurement at 10 K. A hot air blower and a helium flow cryostat were used for temperatures above and below RT, respectively. The measured SR diffractograms covered the $3° < 2\theta < 27°$ range which corresponds to the $0.8 \text{Å}^{-1} < Q < 7.6 \text{Å}^{-1}$ scattering vector range. Each data set was collected for about 1 h.

Powder X-ray diffraction data sets were collected at RT on a PANalytical Expert Pro system in Bragg–Brentano geometry using $CuK_{\alpha1,2}$ ($\lambda = 1.540598, 1.544426$ Å) radiation. The powder diffractograms covered the $22° < 2\theta < 122°$ range with 0.0167° steps.

All powder diffraction data sets were analysed using the Rietveld refinement software package FullProf [31]. The RT structures were refined simultaneously against powder neutron, synchrotron X-ray and $CuK_{\alpha1,2}$ X-ray diffraction patterns employing a weighting scheme of 0.6, 0.2 and 0.2, respectively. A combination of both neutron and X-ray diffraction is very convenient for studies of the distribution of Cu, Mn and O ions in the lattice because of large

differences of the coherent scattering lengths (neutrons) and the atomic form factors (X-rays) for these elements.

3. Experimental results

3.1. Crystal structure of $CaCu_xMn_{7-x}O_{12}$ for different x values at RT

The results of the simultaneous Rietveld refinement of both neutron and X-ray powder diffraction data of $CaCu_{0.10}Mn_{6.90}O_{12}$ at RT obtained with FullProf [31] are shown in Figs. 2a and b. The stoichiometry parameter was determined as $x = 0.10(1)$ for the first sample (labelled as $CaCu_{0.10}Mn_{6.90}O_{12}$) and $x = 0.20(1)$ for the second one (labelled as $CaCu_{0.20}Mn_{6.80}O_{12}$). The resulting parameters of the trigonal structure of $CaCu_{0.10}Mn_{6.90}O_{12}$ and $CaCu_{0.20}Mn_{6.80}O_{12}$ are shown in Table 2.

The grain size and internal strain contributions to Bragg peaks broadening in SR diffraction data have been estimated with the Williamson–Hall method. The instrumental contribution to the peak width has been subtracted
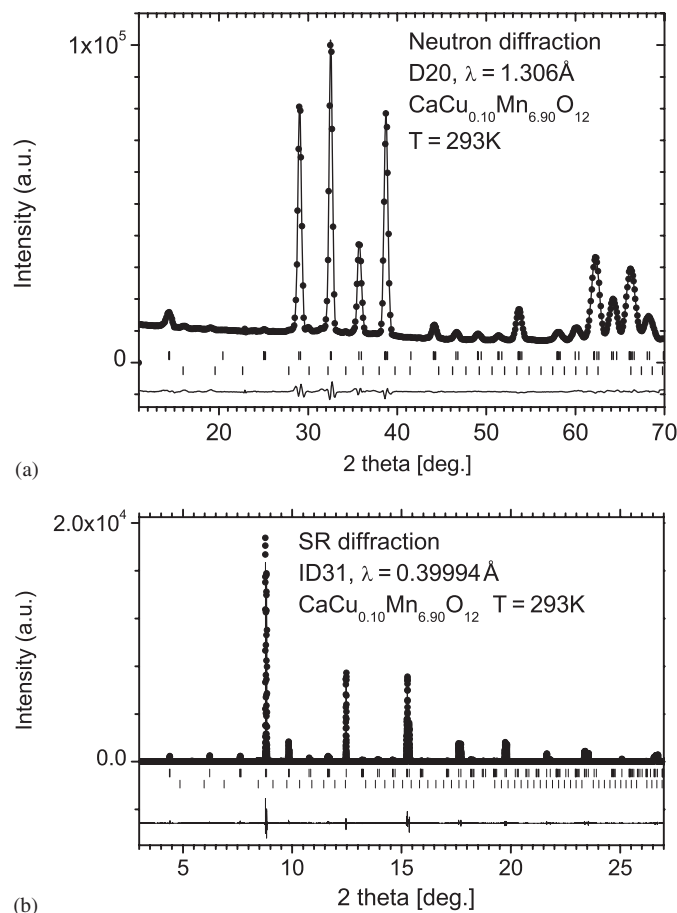

(a)

(b)

Fig. 2. Results of the Rietveld refinement of the neutron (a) and SR (b) powder diffraction pattern of $CaCu_{0.10}Mn_{6.90}O_{12}$ at RT. The solid circles represent measured data, while the solid line represents the calculated diffraction pattern. Below the graph there is a difference curve. The ticks indicate the positions for the Bragg peaks due to the crystal structure of $CaCu_{0.10}Mn_{6.90}O_{12}$ (upper) and Mn_2O_3 (lower).

Table 2
Structural parameters of $CaCu_{0.10}Mn_{6.90}O_{12}$ and $CaCu_{0.20}Mn_{6.80}O_{12}$ determined from simultaneous Rietveld analysis of neutron, SR and $CuK_{\alpha,1,2}$ X-ray powder diffraction data measured at RT

Parameter	$CaCu_{0.10}Mn_{6.90}O_{12}$	$CaCu_{0.20}Mn_{6.80}O_{12}$
Cu content x	0.10(1)	0.20(1)
a (Å)	10.44795(6)	10.43340(14)
c (Å)	6.34327(4)	6.34679(9)
x_{O1}	0.22293(41)	0.22395(76)
y_{O1}	0.27260(40)	0.27030(76)
z_{O1}	0.08165(57)	0.08143(128)
x_{O2}	0.34375(50)	0.34607(2)
y_{O2}	0.52233(45)	0.52288(82)
z_{O2}	0.34067(84)	0.34156(138)
$B_{Ca,Cu,Mn}$ (Å^2)	0.359(24)	0.357(31)
B_O (Å^2)	0.574(28)	0.483(39)
R_p (%)	4.51; 18.5; 13.8	6.89; 14.5; 17.9
R_{wp} (%)	4.67; 25.3; 7.71	6.41; 18.9; 12.0
R_{exp} (%)	1.79; 12.5; 6.71	1.90; 5.34; 7.24
R_B (%)	1.44; 4.07; 4.70	3.09; 4.24; 10.2
χ^2 (%)	6.82; 4.13; 1.322	11.4; 12.55; 2.747

There was one isotropic Debye–Waller factor assumed for the cations, and another one for the oxygen. The reliability factors values from neutron, SR and $CuK_{\alpha,1,2}$ X-rays are shown on left, centre and right side of each column, respectively. The Bragg R-factors R_B refer to the $CaCu_xMn_{7-x}O_{12}$ trigonal phase only.

by using the reference LaB_6 measurements. The values of the internal strain ε vary between 0.03% and 0.05%, i.e. they are less strained than our earlier $CaMn_7O_{12}$ samples as shown in [12]. The grain size estimation based on the Williamson–Hall method has large statistical errors, so in order to compare with earlier results we use the Scherrer formula for the two most intense Bragg peaks observed near $2\theta = 8.8°$. The grain sizes are: 350, 230 and 150 nm for $CaCu_xMn_{7-x}O_{12}$ with $x = 0, 0.10$ and 0.20, respectively. The same method applied to our earlier $CaCu_xMn_{7-x}O_{12}$ studies gives 150 and 110 nm for $x = 0$ [11] and $x = 0.38$ [28], respectively. It is very important that the $CaCu_xMn_{7-x}O_{12}$ samples used in present studies have larger grain sizes and smaller internal strains as those measured earlier [11,12,28]. Our present studies provide information about the phase separation at larger length scales.

Weak impurity peaks in the SR powder diffraction patterns of $CaCu_{0.10}Mn_{6.90}O_{12}$ and $CaCu_{0.20}Mn_{6.80}O_{12}$ are due to the presence of 1.1(2)% and 2.9(4)% by mass of Mn_2O_3 phase, respectively. There were also other weak Bragg peaks which cannot be due to Mn_3O_4 or marokite $CaMn_2O_4$ impurity phases which were found in other $CaCu_xMn_{7-x}O_{12}$ samples (see e.g. [16]). We were not able to identify the impurity phases. The positions of the most intense unindexed Bragg maxima are $Q = 2.31$ and $2.60\,\text{Å}^{-1}$.

Table 3 compares the structural parameters obtained in the present study for $x = 0, 0.10, 0.20$ with literature data for $x = 0.38$ [28] $CaCu_xMn_{7-x}O_{12}$. The unit cell volume,

Table 3
Values of the lattice parameters a_h, c_h of the trigonal structure of several $CaCu_xMn_{7-x}O_{12}$ compounds observed at RT given in the hexagonal setting of the space group $R\bar{3}$

	$x = 0$	$x = 0.10$	$x = 0.20$	$x = 0.38$
a_h (Å)	10.45796(5)	10.44795(6)	10.43340(14)	10.39776
c_h (Å)	6.34197(4)	6.34327(4)	6.34679(9)	6.36338
a_h/c_h	1.649008(13)	1.647092(18)	1.643886(32)	1.63400
α_c (deg.)	90.37156(30)	90.32742(42)	90.25338(74)	90.02354
V_{hex} (Å^3)	600.687(6)	599.661(6)	598.324(14)	595.80000
a_{eff} (Å)	7.3708(8)	7.3666(8)	7.3620(8)	7.35083

α_c is the pseudo-cubic angle, V_{hex} is the hexagonal unit cell volume. The 'effective cubic lattice parameter' a_{eff} is calculated as: $a_{eff} = \sqrt[3]{\frac{2}{3}V_{hex}}$ in order to compare with the cubic lattice parameters observed at higher Cu contents x.

V_{hex} and the a_h-lattice parameter decrease with increasing Cu content, x, in agreement with other structural studies of $CaCu_xMn_{7-x}O_{12}$ for $x \geqslant 0.5$ [9,26]. The c_h-lattice parameter increases with increasing x. The degree of the pseudo-cubic distortion of the trigonal phase is estimated from the pseudo-cubic angle α_c which is calculated as (see e.g. [11])

$$\cos\alpha_c = \frac{1 - \frac{3}{8}(a_h/c_h)^2}{1 + \frac{3}{4}(a_h/c_h)^2}.$$

With increasing x, the (a_h/c_h) ratio approaches $\sqrt{\frac{8}{3}} \approx 1.63299$ and the pseudo-cubic angle α_c approaches $90.0°$. In order to compare our present results with earlier $CaCu_xMn_{7-x}O_{12}$ structural studies [9,26] we have calculated an effective cubic lattice parameter a_{eff} related to the observed hexagonal[1] unit cell volume by the relation $V_{hex} = \frac{3}{2}a_{eff}^3$. The x dependence of a_{eff} reported here for $0 \leqslant x \leqslant 0.38$, shown in Table 3, is linear with a slope of about $\Delta a/\Delta x = 0.06\,\text{Å}$ per unit x, and agrees well with literature values of the cubic lattice constant of $CaCu_xMn_{7-x}O_{12}$ for $x \geqslant 0.5$ reported by [9,26].

The Mn, Cu and O positional parameters obtained from Rietveld analysis of present neutron diffraction data for $CaCu_xMn_{7-x}O_{12}$ with $x = 0, 0.10$ and 0.20 have been used to calculate the Mn–O and Cu–O bond lengths. The resulting values are given in Table 4 and show the influence of the Cu concentration on the Jahn–Teller effect in the $CaCu_xMn_{7-x}O_{12}$ system. The structural parameters determined for $CaMn_7O_{12}$ in the present study agree within 2σ statistical errors with those reported in [16].

The apical MnO_6 octahedra compression with four long and two short Mn–O bonds corresponds to the $(x^2 - y^2)$-type orbitals, see e.g. [10], and is observed in all the compositions studied. The $CaCu_xMn_{7-x}O_{12}$ family is

---

[1]The structure of $CaMn_7O_{12}$ at RT has been erroneously reported to be cubic, with $a = 7.3768\,\text{Å}$, by Sanchez-Benitez et al. [26] who finally confirmed in the erratum [32] that the structure is trigonal at RT.

unique among other manganite perovskites, see e.g. [10], in which the MnO_6 Jahn–Teller distortion leads usually to four short and two long Mn–O bonds corresponding to a $(3z^2 - r^2)$-type orbital. The values of the Jahn–Teller distortion mode Q_3 [33] and the bond length dispersion Δ (see e.g. [34]) decrease when x increases in agreement with the tendency towards the undistorted cubic structure for larger Cu content.

3.2. Phase coexistence in $CaCu_xMn_{7-x}O_{12}$ above RT

The SR powder diffraction patterns of $CaMn_7O_{12}$ show a similar phase separation phenomenon as observed earlier with samples composed of smaller grains [11,12]. The

Table 4
Values of bond lengths and bond angles obtained from neutron diffraction data for the trigonal phase (space group $R\bar{3}$) of $CaCu_xMn_{7-x}O_{12}$ compounds with $x = 0, 0.10$ and 0.20 at RT

	Pos ($R\bar{3}$)	$x = 0$	$x = 0.10$	$x = 0.20$
Mn–O (l) × 2	(9d)	2.049(10)	2.031(4)	2.008(5)
Mn–O (m) × 2	(9d)	2.031(7)	2.030(6)	1.999(7)
Mn–O (s) × 2	(9d)	1.889(7)	1.898(4)	1.914(8)
$Q_2 = l - m$	(9d)	0.017(12)	0.001(7)	0.009(7)
$Q_3 = 2s - l - m$	(9d)	−0.302(16)	−0.265(9)	−0.179(16)
$\Delta \times 10^4$	(9d)	12.9(2.6)	10.9(1.4)	11.0(3.1)
Mn–O × 6	(3b)	1.894(9)	1.915(5)	1.924(5)
Mn/Cu–O × 2	(9e)	1.931(8)	1.916(4)	1.934(9)
Mn/Cu–O × 2	(9e)	1.923(6)	1.916(4)	1.928(1)

The long (l), middle (m) and short (s) Mn^{3+}–O bond lengths for the Jahn–Teller distorted surrounding of Mn^{3+} ions located in (9d) positions. Q_2 and Q_3 are Jahn–Teller distortion modes and $\Delta = \frac{1}{3}\sum_{i=1,3} \{(d_i - \langle d \rangle)/\langle d \rangle\}^2$, where $\langle d \rangle$ is the average Mn–O bond length, as used in [34].

Bragg peaks for the trigonal and cubic phases are narrow for all measured temperatures (grain size about 350 nm based on the Scherrer equation). Our goal was to determine if this also holds for smaller Cu concentrations in $CaCu_xMn_{7-x}O_{12}$. Representative parts of the SR powder diffraction patterns, containing the strongest measured Bragg peaks and the fitted pattern profile (Rietveld method) near $2\theta = 8.8°$, for $CaCu_{0.10}Mn_{6.90}O_{12}$ and $CaCu_{0.20}Mn_{6.80}O_{12}$ are shown in Figs. 3a and b, respectively. The sharp Bragg peaks of the trigonal and cubic phases are clearly separated. The domain sizes of both phases observed in $CaCu_{0.10}Mn_{6.90}O_{12}$ and $CaCu_{0.20}Mn_{6.80}O_{12}$ at 330 K and above (estimated from the Scherrer formula) are at least 200 nm. The $CaCu_{0.10}Mn_{6.90}O_{12}$ SR diffraction pattern shows a single trigonal phase at RT. The RT $CaCu_{0.20}Mn_{6.80}O_{12}$ SR diffraction pattern cannot be described by a single trigonal phase; there is an excess of intensity between the narrow Bragg peaks as shown in Fig. 3b (see plot for $T = 293$ K). This additional contribution can be due to a cubic phase described within the space group $Im\bar{3}$, similar to that observed in the parent $CaMn_7O_{12}$ compound above 450 K [11]. It was assumed that this cubic phase contributes to broad diffraction maxima due to limited grain size and/or strains. Based on Rietveld refinements at RT the cubic phase contributes 28 vol% in $CaCu_{0.20}Mn_{6.80}O_{12}$. The existence of this cubic phase in $CaCu_{0.20}Mn_{6.80}O_{12}$ was also investigated at low temperatures. Even at low temperatures down to 10 K the SR diffraction pattern of $CaCu_{0.20}Mn_{6.80}O_{12}$ indicated 21 vol% of the cubic phase. A similar phenomenon was already observed in $CaCu_xMn_{7-x}O_{12}$ systems at higher doping $x = 0.38$ [28], where at low temperatures down to 10 K the cubic and trigonal phases occupy about 70% and 30% of the volume, respectively.
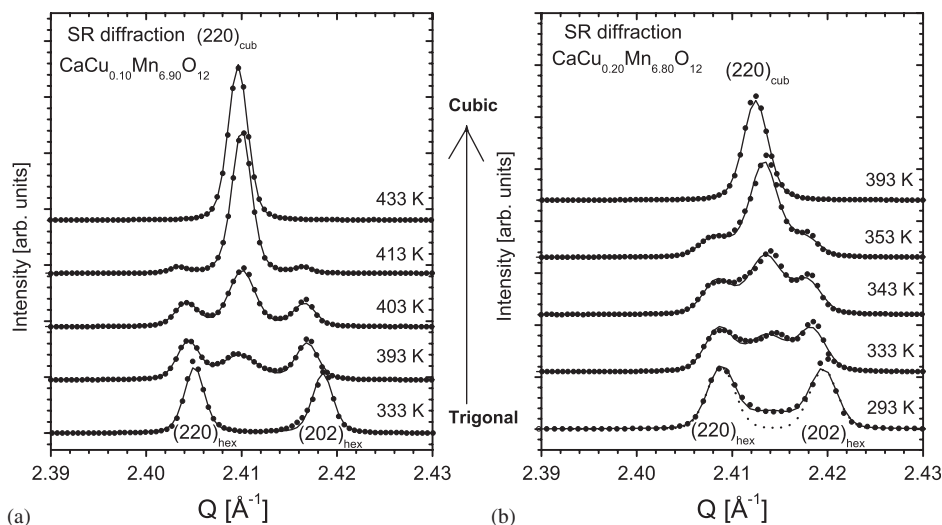

Fig. 3. Representative parts of the SR powder diffraction patterns of $CaCu_{0.10}Mn_{6.90}O_{12}$ (a) and $CaCu_{0.20}Mn_{6.80}O_{12}$ (b) with the most intense Bragg peaks located near $2\theta = 8.8°$ (see Fig. 2b). Solid circles represent measured data and the lines are the profiles obtained from Rietveld refinements. Q is the length of the scattering vector calculated as $Q = (4\pi/\lambda)\sin\theta$, where the scattering angle is 2θ. The patterns measured at different temperatures are vertically shifted for clarity. The dashed line on the $CaCu_{0.20}Mn_{6.80}O_{12}$ pattern at RT shows the contribution of the trigonal phase only.

The temperature dependence of the hexagonal a_h-, c_h- and cubic, a_c-lattice parameters obtained from Rietveld refinements of the $CaCu_{0.10}Mn_{6.90}O_{12}$ and $CaCu_{0.20}Mn_{6.80}O_{12}$ SR diffraction patterns is shown in Figs. 4a–f, respectively. The thermal expansion of both compositions is highly anisotropic: a_h is increasing and concave upward, while c_h has a maximum and an inflection point. There is a clear coexistence of the trigonal and cubic phases with a weak hysteresis of all three lattice parameters, as observed in $CaMn_7O_{12}$ [11,12].

The temperature dependence of the pseudo-cubic angle α_c and the concentration of the cubic phase for $CaCu_{0.10}Mn_{6.90}O_{12}$ and $CaCu_{0.20}Mn_{6.80}O_{12}$ are shown in Figs. 5a and b, respectively. The concentration of the cubic phase is defined as the total volume occupied by the cubic phase divided by the sum of the volumes of both cubic and trigonal phases. The most important effect observed for both compounds is a minimum of α_c at a temperature when the cubic phase concentration becomes larger than 50%. Such changes of the trigonal phase structure were already observed in $CaMn_7O_{12}$ [11]. The nearly linear decrease of α_c observed in $CaCu_{0.10}Mn_{6.90}O_{12}$ and $CaCu_{0.20}Mn_{6.80}O_{12}$ by about 0.30° on warming by 50 K (i.e. at temperatures before the minimum of α_c) is much larger than that observed for the undoped $CaMn_7O_{12}$, where this change was only 0.07° per 50 K [11,12].

The temperature dependence of the unit cell volumes (normalized to three formula units) of the hexagonal and cubic phases of $CaCu_{0.10}Mn_{6.90}O_{12}$ and $CaCu_{0.20}Mn_{6.80}O_{12}$ is shown in Figs. 6a and b, respectively. The $CaCu_{0.20}Mn_{6.80}O_{12}$ sample shows the same behaviour as the parent ($x = 0$) [11,12] and the $x = 0.38$ [28] $CaCu_xMn_{7-x}O_{12}$ compounds, i.e. the unit cell volume of the cubic phase is smaller than that of the trigonal phase. The higher density of the cubic phase has been attributed to its charge delocalized electronic ground state, while the smaller density of the trigonal phase has been attributed to the charge ordered state of $CaMn_7O_{12}$ [11]. This interpretation was supported by a considerable change of the resistivity at the trigonal to cubic phase transition in $CaMn_7O_{12}$ [13]. The $CaCu_{0.10}Mn_{6.90}O_{12}$ compound shows a reversed behaviour, i.e. the unit cell volume of the cubic phase is larger than that of the trigonal phase.

The different unit cell volumes for the cubic and trigonal phases (see Fig. 6) can be readily identified in Fig. 3. The $(2\,2\,0)_{cub}$ peak position for $CaCu_{0.10}Mn_{6.90}O_{12}$ is shifted to low Q-values and overlaps with the low Q $(2\,2\,0)_{hex}$ Bragg peak. Whereas in $CaCu_{0.20}Mn_{6.80}O_{12}$ the cubic peak shifts to higher Q values and overlaps with the high Q $(2\,0\,2)_{hex}$ peak. This relative shift of the cubic peak with respect to the trigonal peaks indicates a considerable relative change in the unit cell volumes as one goes from $CaCu_{0.10}Mn_{6.90}O_{12}$ to $CaCu_{0.20}Mn_{6.80}O_{12}$.
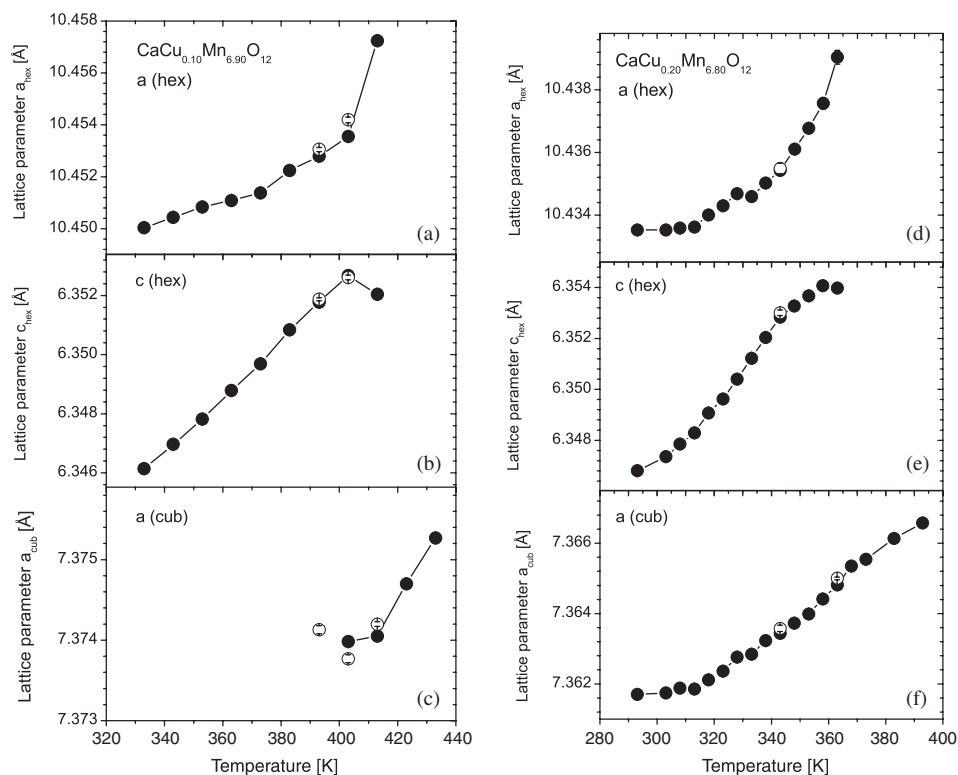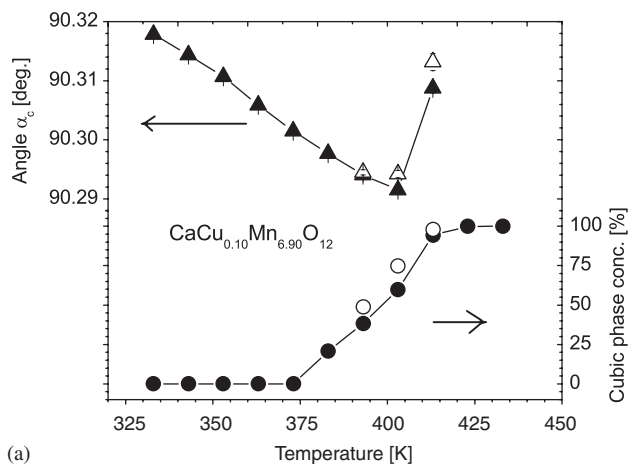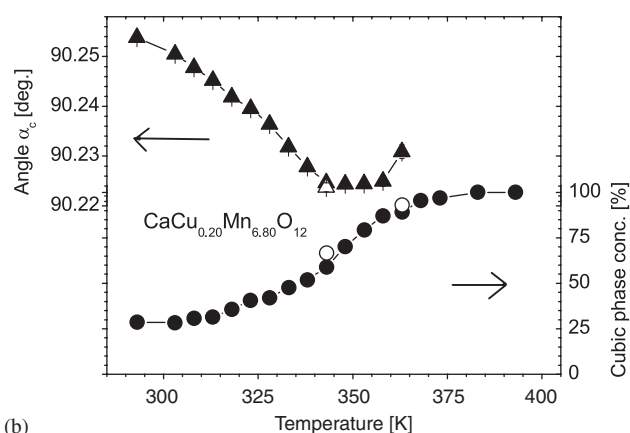

Fig. 4. Temperature dependence of the hexagonal lattice parameters a_h, c_h and cubic lattice parameter a_c obtained from $CaCu_{0.10}Mn_{6.90}O_{12}$ SR diffraction data is shown in panels a, b and c, respectively. Temperature dependence of the hexagonal lattice parameters a_h, c_h and cubic lattice parameter a_c obtained from $CaCu_{0.20}Mn_{6.80}O_{12}$ SR diffraction data is shown in panels d, e and f, respectively. The full symbols show values measured on warming while the open symbols those on cooling.
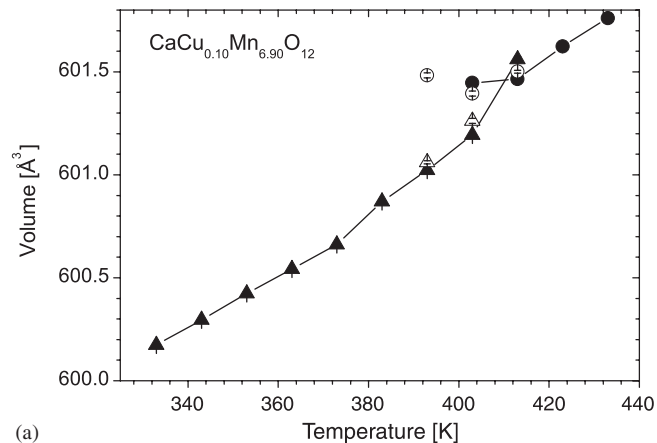
Fig. 5. Temperature dependence of the pseudo-cubic angle α_c (triangles) together with the cubic phase concentration (circles) for $CaCu_{0.10}Mn_{6.90}O_{12}$ and $CaCu_{0.20}Mn_{6.80}O_{12}$ are shown in panels a and b, respectively. The full symbols show values measured on warming while the open symbols those on cooling.

Fig. 6. Temperature dependence of the unit cell volume of the trigonal (triangles) and cubic (circles) phases for $CaCu_{0.10}Mn_{6.90}O_{12}$ are and $CaCu_{0.20}Mn_{6.80}O_{12}$ are shown in panels a and b, respectively. The unit cell volumes have been normalized to three formula units as in [11,12]. The full symbols show values measured during heating and the open symbols were measured during cooling.

4. Phase segregation in $CaCu_xMn_{7-x}O_{12}$
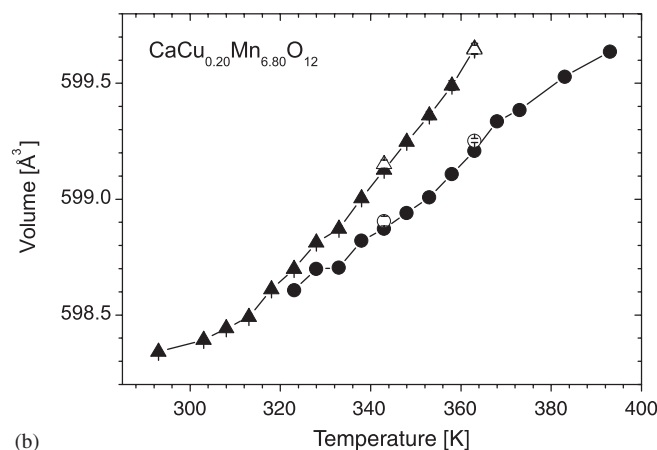
A schematic phase diagram showing the different phases of $CaCu_xMn_{7-x}O_{12}$ compounds as a function of temperature and copper concentration is shown in Fig. 7. It is based on present results as well as earlier studies [11,12,28]. Between $x = 0$ [11,12] and $x = 0.20$ there are three distinct regions with: (i) a single cubic phase at high temperature, (ii) a mixture of trigonal + cubic phases at intermediate temperature and (iii) a single trigonal phase at low temperature. Between $x = 0.20$ and 0.38 one observes a single cubic phase at high temperature and coexisting large domains of both trigonal and cubic phases at lower temperatures. Above $x = 0.7$ [28] there is only a cubic phase at all temperatures.

5. Conclusions

The Jahn–Teller distortion of the trigonal phase observed in the $CaCu_xMn_{7-x}O_{12}$ system with $x \leqslant 0.25$ confirms the charge ordering assumption derived from $CaMn_7O_{12}$ [10]. The degree of the apical Jahn–Teller distortion for Mn^{3+} ions in $(9d)$ positions decreases with increasing x. The structural transition observed in $CaCu_{0.10}Mn_{6.90}O_{12}$ and $CaCu_{0.20}Mn_{6.80}O_{12}$ is similar to that observed in the undoped $CaMn_7O_{12}$ [11,12]. The important result is that the domain size of the separated phases is at least 350 nm for $x = 0$ and 200 nm for $x = 0.10$ and 0.20. The transition temperatures depend on the Cu content x. Therefore, the phase coexistence temperature range for this interesting class of materials can be controlled through Cu doping. Applications of these materials in electronics are possible due to the rapid changes in dielectric and magnetoresistive properties of these manganites as a function of copper substitution.

The main features of the phase transition are summarized below:

- The phase separation leads to the coexistence of relatively large domains of the cubic and trigonal phases with a size above 200 nm.
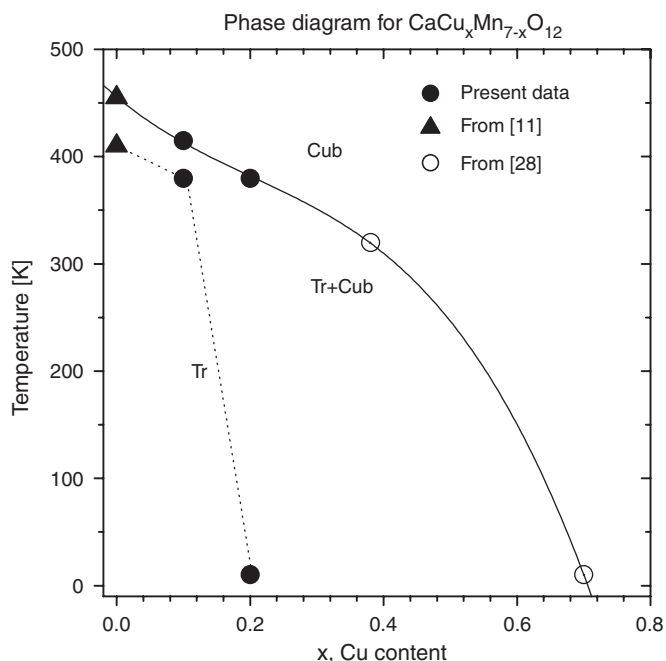
Phase diagram for CaCu$_x$Mn$_{7-x}$O$_{12}$

Fig. 7. Schematic phase diagram for the CaCu$_x$Mn$_{7-x}$O$_{12}$ compounds with $0 \leqslant x \leqslant 0.7$. The cubic phase (space group $Im\bar{3}$) is denoted by (Cub), the trigonal phase (space group $R\bar{3}$) is denoted by (Tr). The region with a coexistence of both trigonal and cubic phases is denoted by (Tr + Cub). The transition temperatures are derived from present data (solid circles) and [11] (solid triangles) and [28] (empty circles). The lines are shown to guide the eye.

- The volume occupied by the cubic phase increases at the expense of the volume occupied by the trigonal phase as temperature increases.
- The pseudo-cubic angle α_c characterizing the distortion of the trigonal phase has a minimum at the temperature when the trigonal phase starts to become the minority phase, i.e. when this phase occupies less than 50% of the volume.

There is however one important difference between the unit cell sizes of the coexisting phases observed in CaCu$_{0.10}$Mn$_{6.90}$O$_{12}$ and CaCu$_{0.20}$Mn$_{6.80}$O$_{12}$. The unit cell volumes of the trigonal and cubic phases behave differently in CaCu$_{0.10}$Mn$_{6.90}$O$_{12}$ and CaCu$_{0.20}$Mn$_{6.80}$O$_{12}$ (see Figs. 6a, b). This result suggests that the electronic properties of the trigonal and cubic phases CaCu$_x$Mn$_{7-x}$O$_{12}$ may depend on the x content and that the assumption of charge ordering and charge delocalization derived from CaMn$_7$O$_{12}$ studies [11,13] should be studied in more detail for compositions in the vicinity of $x = 0.10$.

Electronic transport studies have shown that CaCu$_x$Mn$_{7-x}$O$_{12}$ compounds with $x \leqslant 1$ are semiconductors [9]. The undoped CaMn$_7$O$_{12}$ compound is also semiconducting but its conductivity jumps abruptly by an order of magnitude at the trigonal to cubic transition temperature region. It would be interesting to verify if these low Cu-doped CaCu$_x$Mn$_{7-x}$O$_{12}$ samples also show considerable changes of the resistivity, bulk modulus and

infrared absorption in the phase transition region. It would be also interesting to study the influence of the Cu doping on the colossal dielectric constants observed in undoped CaMn$_7$O$_{12}$ [17].

Acknowledgments

References

[1] E. Dagotto, T. Hotta, A. Moreo, Phys. Rep. 344 (2001) 1.
[2] G.H. Jonker, J.H. Van Santen, Physica (Utrecht) 16 (1950) 337.
[3] T. Lottermoser, T. Lonkai, U. Amann, D. Hohlwein, J. Ihringer, M. Fiebig, Nature 430 (2004) 541.
[4] T. Kimura, T. Goto, H. Shintani, K. Ishizaka, T. Arima, Y. Tokura, Nature 426 (2003) 55.
[5] P. Lunkenheimer, V. Bobnar, A.V. Pronin, A.I. Ritus, A.A. Volkov, A. Loidl, Phys. Rev. B 66 (2002) 052105.
[6] Z. Zeng, M. Greenblatt, M.A. Subramanian, M. Croft, Phys. Rev. Lett. 82 (1999) 3164.
[7] J. Sánchez-Benitez, J.A. Alonso, M.J. Martinez-Lope, M.T. Casais, J.L. Martinez, A. de Andrés, M.T. Fernandez-Diaz, Chem. Mater. 15 (2003) 2193.
[8] E.A. Pomerantseva, D.M. Itkis, E.A. Goodilin, J.G. Noudem, M.V. Lobanov, M. Greenblatt, Yu.D. Tratyakov, J. Mater. Chem. 14 (2004) 1450.
[9] Z. Zeng, M. Greenblatt, J.E. Sunstrom, M. Croft, S. Khalid, J. Solid State Chem. 147 (1999) 185.
[10] B. Bochu, J.L. Buevoz, J. Chenavas, A. Collomb, J.C. Joubert, M. Marezio, Solid State Commun. 36 (1980) 133.
[11] R. Przeniosło, I. Sosnowska, E. Suard, A. Hewat, A.N. Fitch, J. Phys. Condens. Matter 14 (2002) 5747.
[12] R. Przeniosło, W. van Beek, I. Sosnowska, Solid State Commun. 126 (2003) 485.
[13] I.O. Troyanchuk, A.N. Chobot, Crystallogr. Rep. 42 (1997) 983.
[14] S.N. Ruddlesden, D. Popper, Acta Crystallogr. 10 (1951) 538.
[15] W. Kobayashi, I. Terasaki, M. Mikami, R. Funahashi, T. Nomura, T. Katsufuji, arXiv: cond-mat/0402032, 2004.
[16] R. Przeniosło, I. Sosnowska, E. Suard, A. Hewat, A.N. Fitch, Physica B 344 (2004) 358.
[17] S. Yañez Vilar, A. Castro-Couceiro, B. Rivas-Murias, A. Fondado, J. Mira, J. Rivas, M.A. Señaris-Rodriguez, Z. Anorg. Allg. Chem. 631 (2005) 2192.
[18] R. Przeniosło, I. Sosnowska, D. Hohlwein, T. Hauß, I.O. Troyanchuk, Solid State Commun. 111 (1999) 687.
[19] A. Prodi, G. Allodi, E. Gilioli, F. Licci, M. Marezio, F. Bolzoni, A. Gauzzi, R. De Renzi, Physica B 374–375 (2006) 55.
[20] R. Przeniosło, I. Sosnowska, P. Strunz, D. Hohlwein, T. Hauß, I.O. Troyanchuk, Physica B 276–278 (2000) 547.
[21] R. Przeniosło, I. Sosnowska, M. Żółtek, D. Hohlwein, I.O. Troyanchuk, Physica B 241–243 (1998) 730.
[22] O. Volkova, Yu. Arango, N. Tristan, V. Kataev, E. Gudilin, D. Meier, T. Lorenz, B. Büchner, A. Vasil'ev, JETP Lett. 82 (2005) 444.
[23] R. Przeniosło, JETP Lett. 83 (2006) 221.
[24] O. Volkova, Yu. Arango, N. Tristan, V. Kataev, E. Gudilin, D. Meier, T. Lorenz, B. Büchner, A. Vasil'ev, JETP Lett. 83 (2006) 222.
[25] I.O. Troyanchuk, L.S. Lobanovsky, N.V. Kasper, M. Hervieu, A. Maignan, C. Michel, H. Szymczak, A. Szewczyk, Phys. Rev. B 58 (1998) 14903.

[26] J. Sánchez-Benitez, C. Prieto, A. de Andrés, J.A. Alonso, M.J. Martinez-Lope, M.T. Casais, Phys. Rev. B 70 (2004) 024419.

[27] J. Chenavas, J.C. Joubert, M. Marezio, B. Bochu, J. Solid State Chem. 14 (1975) 25.

[28] R. Przeniosło, I. Sosnowska, W. Van Beek, E. Suard, A. Hewat, J. Alloys Compd. 362 (2004) 218.

[29] R. Przeniosło, M. Regulski, I. Sosnowska, R. Schenider, J. Phys. Condens. Matter 14 (2002) 1061.

[30] E.A. Pomerantseva, D.M. Itkis, M.V. Makarova, M.B. Lobanov, N.N. Oleinikov, Yu.D. Tret'yakov, Dokl. Chem. 388 (2003) 33–37.

[31] J. Rodríguez-Carvajal, Physica B 192 (1992) 55.

[32] J. Sánchez-Benitez, et al., Phys. Rev. B 71 (2005) 059901(E).

[33] J.H. Van Vleck, J. Chem. Phys. 7 (1939) 72.

[34] J. Rodriguez-Carvajal, M. Hennion, F. Moussa, A.H. Moudden, L. Pinsard, A. Revcolevschi, Phys. Rev. B 57 (1998) R3189.